

A mechanically strong and ductile soft magnet with ultralow coercivity

Dierk Raabe (✉ d.raabe@mpie.de)

Max-Planck-Institut für Eisenforschung <https://orcid.org/0000-0003-0194-6124>

Liuliu Han

Max-Planck-Institut für Eisenforschung GmbH

Fernando Fernando

Department of Material Science, Technical University of Darmstadt

Isnaldi Souza Filho

Max-Planck-Institut für Eisenforschung <https://orcid.org/0000-0002-5761-4981>

Nicolas Peter

Forschungszentrum Jülich

Ye Wei

Max-Planck-Institut für Eisenforschung

Baptiste Gault

Max Planck Institute for Iron Research <https://orcid.org/0000-0002-4934-0458>

Oliver Gutfleisch

Department of Material Science, Technical University of Darmstadt

Zhiming Li

Central South University <https://orcid.org/0000-0002-8170-5621>

Physical Sciences - Article

Keywords:

Posted Date: December 10th, 2021

DOI: <https://doi.org/10.21203/rs.3.rs-1145535/v1>

License:   This work is licensed under a Creative Commons Attribution 4.0 International License.

[Read Full License](#)

Version of Record: A version of this preprint was published at Nature on August 10th, 2022. See the published version at <https://doi.org/10.1038/s41586-022-04935-3>.

A mechanically strong and ductile soft magnet with ultralow coercivity

Liuliu Han¹, Fernando Maccari², Isnaldi R. Souza Filho¹, Nicolas J. Peter¹, Ye Wei¹, Baptiste Gault¹, Oliver Gutfleisch², Zhiming Li^{1,3}, Dierk Raabe¹

¹*Max-Planck-Institut für Eisenforschung, Max-Planck-Straße 1, 40237 Düsseldorf, Germany*

²*Department of Material Science, Technical University of Darmstadt, 64287 Darmstadt, Germany*

³*School of Materials Science and Engineering, Central South University, 410083 Changsha, China*

*Correspondence to lizhiming@csu.edu.cn (Z.L.), d.raabe@mpie.de (D.R.)

Soft magnetic materials (SMMs) are indispensable components in electrified applications and sustainable energy supply, allowing permanent magnetic flux variations in response to high frequency changes of the applied magnetic field, at lowest possible energy loss¹. The global trend towards electrification of transport, households and manufacturing leads to a massive increase in energy consumption due to hysteresis losses². Therefore, minimizing coercivity, which scales the losses in SMMs, is crucial³. Yet, meeting this target alone is not enough: SMMs used for instance in vehicles and planes must withstand severe mechanical loads, i.e., the alloys need high strength and ductility⁴. This is a fundamental design challenge, as most methods that enhance strength introduce stress fields that can pin magnetic domains, thus increasing coercivity and hysteretic losses⁵. Here, we introduce a new approach to overcome this dilemma. We have designed a Fe-Co-Ni-Ta-Al multicomponent alloy with ferromagnetic matrix and paramagnetic coherent nanoparticles of well-controlled size (~91 nm) and high volume fraction (55%). They impede dislocation motion, enhancing strength and ductility. Yet, their small size, low coherency stress and small magnetostatic energy create an interaction volume below the magnetic domain wall width, leading to minimal domain wall pinning, thus maintaining the material's soft magnetic properties. The new material exhibits an excellent combination of mechanical and magnetic properties outperforming other multicomponent alloys and conventional SMMs. It has a tensile strength of ~1336 MPa at 54% tensile elongation, an extremely low coercivity of ~78 A/m (<1 Oe) and a saturation magnetization of ~100 Am²/kg. The work opens new perspectives on developing magnetically soft and mechanically strong and ductile materials for the sustainable electrification of industry and society.

Lowest possible coercivity is a primary goal for soft magnetic materials (SMMs), to reduce hysteresis-related energy losses, noise, heating and the associated material damage¹⁻³. Also, new SMMs with higher strength and ductility are needed, to operate under mechanically demanding loading conditions for safety-critical parts in transportation and energy⁴. This multi-property profile creates a fundamental dilemma. Mechanical strength of metallic materials is produced by lattice defects and their elastic interactions with linear lattice faults that carry inelastic deformation, referred to as dislocations. However, the defects also interact with the magnetic domain walls and pin them. The loss in domain wall motion increases coercivity so that the materials lose their soft magnetic features. Therefore, current SMMs follow the design rule of avoiding lattice defects to minimize coercivity⁵. Vice versa, increasing an alloy's mechanical strength requires enhancing its internal stress level through defects such as dislocations, grain boundaries and precipitates⁶. This means that the task of making soft magnets mechanically strong is a trade-off between two mutually exclusive design strategies, namely, mechanical strength vs. unaffected domain wall motion.

The theory of the grain size dependence of coercivity⁷ shows its proportionality to the 6th power of the grain size for the case of nanocrystalline materials, a relation that can be also applied to particles⁸. Current design of SMMs has thus focused on using small particles (<15 nm)^{8,9} and grain sizes (<100 nm)¹⁰⁻¹². According to magnetic strain theory, the coercivity depends on the energy required to displace domain walls to overcome lattice barriers¹³⁻¹⁵. Here we introduce particles into multicomponent massive solid solution matrix and increase their size from the commonly used range of 5~15 nm to 90~100 nm. With that, the internal stress level and the overall elastic coherency misfit energy are reduced through the smaller specific surface area (total surface area per unit of volume) of the particles, caused by the coarsening. We then propose that the particle design must follow four main rules. First, minimal pinning of domain walls requires a well-tuned and -controlled particle size distribution with optimum balance between the decrease in specific surface area and the increase in magnetostatic energy during particle coarsening. Second, the particle size must remain smaller than the domain wall width to prevent strong pinning, i.e. strong resistance against spin rotation⁶. Third, the particles' chemical composition and crystal structure determine their saturation magnetization; therefore, antiferromagnetic elements are usually excluded. Fourth, strengthening of the alloys is determined by the interaction between dislocations and particles and by the friction forces exerted on dislocations in the massive solid

solution matrix. Thus, intrinsically strong intermetallic particles with minimal lattice misfit are employed. These require high forces for dislocation cutting (giving strength), but repeated cutting by ensuing dislocations emitted by the same source shear them with gradual ease along the remaining and gradually reducing particle cross sections (providing ductility).

These different mechanism considerations had next to be translated into a corresponding compositional alloy design concept. This is mainly guided by the requirement for (a) a ferromagnetic matrix with (b) high solid solution contribution, components that trigger the formation of (c) strong and stable intermetallic phases with (d) small lattice misfit relative to the matrix. These considerations have led us to the non-equiatomic iron–nickel–cobalt–tantalum–aluminium ($\text{Co}_{27.7}\text{Fe}_{32.6}\text{Ni}_{27.7}\text{Ta}_{5.0}\text{Al}_{7.0}$, at.%) multicomponent alloy (MCA). We synthesized the material in a vacuum induction melting furnace followed by conventional hot rolling and homogenization (details of the processing procedures and chemical compositions are provided in the Methods section). Through further isothermal heat treatments (1~100 h at 1173 K), we obtain a wide range of particle sizes (24~255 nm). The particles have $L1_2$ structure and a complex composition, as presented in detail below.

Fig. 1 shows the structural characterization of the MCA with medium particle size (M-MCA, where “M” stands for “medium particle size”) after annealing at 1173 K for 5 h. The M-MCA shows an average grain size of $85.3 \pm 25.6 \mu\text{m}$ (including annealing twin boundaries) according to electron backscatter diffraction (EBSD) analysis shown in Fig. 1a. The electron channelling contrast imaging (ECCI) analysis shows that the $L1_2$ particles have a high number density ($7.2 \times 10^{20} \text{m}^{-3}$) and a large volume fraction (~55%) in homogeneous distribution within the face-centered cubic (fcc) matrix (Fig. 1b). The lattice misfit (~0.48%) between the fcc matrix and the $L1_2$ particles has been calculated using their lattice parameters¹⁶ acquired from the X-ray diffraction (XRD) patterns (Fig. 1c) by Rietveld simulation¹⁷. Such a small lattice mismatch reduces the capillary driving forces for further coarsening and the uniform dispersion prevents plastic localization at high strength^{18,19}. The central beam dark-field (DF) transmission electron microscopy (TEM) analysis reveals that the average size of the $L1_2$ particles is $90.8 \pm 35.8 \text{nm}$, Fig. 1d. The corresponding selected-area electron diffraction (SAED, see inset of Fig. 1d) and high-resolution (HR)-TEM (Extended Data Fig. 1d) confirm the high coherency between the particles and the matrix.

The elemental partitioning between the L₁₂ precipitates and fcc solid solution matrix is characterized by atom probe tomography (APT). Fig. 1e shows the three-dimensional (3D) distribution of the volume investigated by APT, highlighted by a set of iso-surfaces delineating regions containing above 25 at.% Fe. Fig. 1f shows the one-dimensional (1D) compositional profiles acquired along the cylinder in Fig. 1e. The profiles show that Fe partitions into the fcc matrix (36 at.%), whereas the L₁₂ particles are enriched in Ni (40 at.%), Ta (13 at.%), and Al (9 at.%). The compositions of the fcc and L₁₂ phases were determined by averaging over 3 APT data sets (including 10 L₁₂ particles) as Fe₃₆Co₂₈Ni₂₆Al₇Ta₃ and Ni₄₀Co₂₆Ta₁₃Fe₁₂Al₉ (at.%), respectively.

Besides these intragranular nanoparticles, we also observed two types of grain-boundary variants: (a) Coarse grain boundary particles (160.2 ± 55.3 nm) with the same crystal structure and composition (Extended Data Fig. 1a-c) as the ones inside the grains; (b) incoherent particles with a minor fraction (<0.3%) at triple-points of the grains with different structure (cubic Fd-3m, Fig. 1c) and composition (Ta_{40.0}Co_{26.1}Fe_{20.1}Ni_{11.1}Al_{2.7}, at.%, Extended Data Fig. 1e). These two types of particles are both promoted by the high diffusion rate along the grain boundaries.

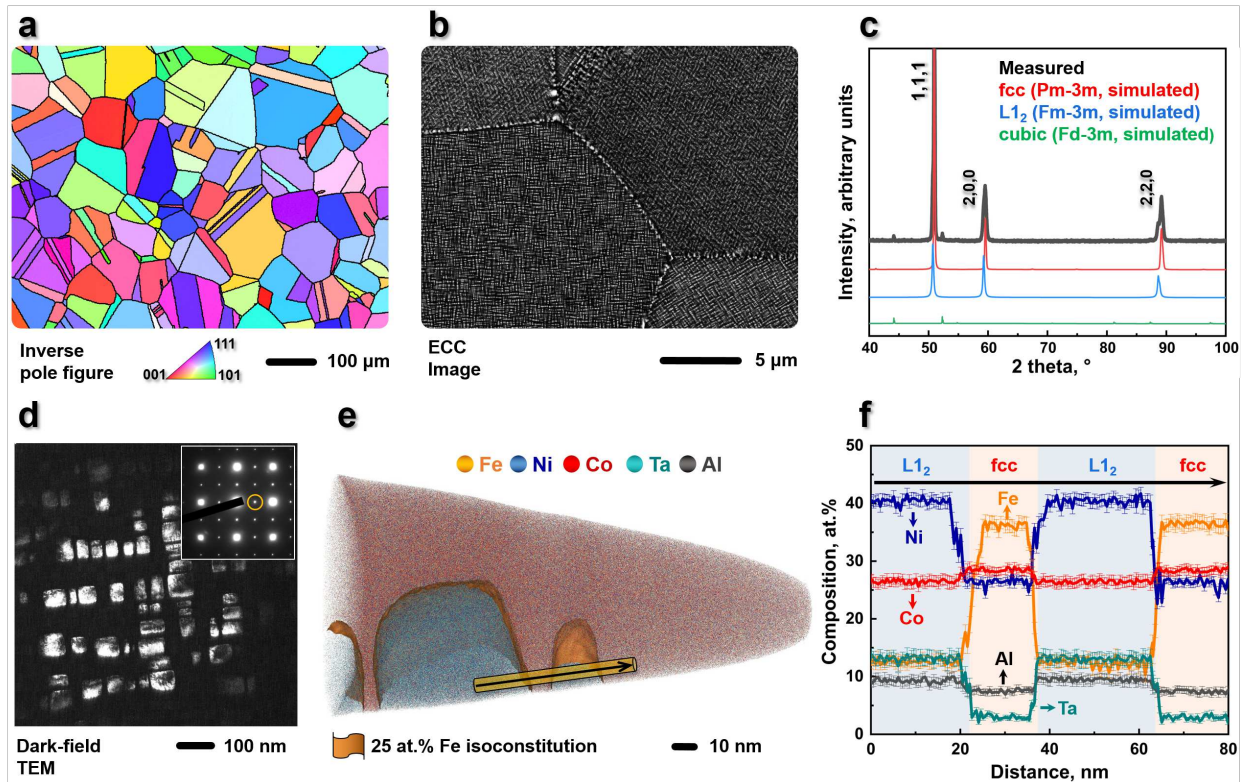


Figure 1 | Microstructure and chemical composition of the M-MCA. **a**, EBSD-inverse pole figure (IPF) map showing the equiaxed grains of the fcc matrix. The black lines highlight the high-angle grain/twin boundaries. **b**, ECC image featuring the high-density uniformly distributed L₁₂ particles in the grain interiors and heterogeneous particles at the grain boundaries. **c**, Measured and simulated XRD patterns showing the phase structures. **d**, Centered dark-field TEM image of the L₁₂ particles obtained using the (011) superlattice spot (see inset). **e**, 3D reconstruction map of a typical APT tip showing the cuboidal L₁₂ particles embedded in the fcc matrix. The L₁₂/fcc interfaces are highlighted using iso-composition surfaces containing 25 at.% Fe. **f**, 1D compositional profiles computed along the cylinder region (marked by black arrow) in **e**, showing the compositional changes across several interfaces. Error bars refer to the standard deviations of the counting statistics in each bin of the profiles.

The current strategy by tuning the particle size also enables overcoming the strength-ductility trade-off, significant for advanced alloys with gigapascal-level strength. Fig. 2a displays the tensile stress-strain curves of the M-MCA at room-temperature (red curve). The yield strength (σ_y) is 904 ± 11 MPa with an ultimate tensile strength (σ_{UTS}) of 1336 ± 21 MPa, and an elongation at fracture (ϵ_f) up to $53.6 \pm 1.5\%$, averaged from four tests. Accordingly, the M-MCA has a high $\sigma_{UTS} \times \epsilon_f$ value of ~ 71.6 GPa%. To reveal the improvement in strength and ductility achieved by the well-controlled particle size distribution, the mechanical response of a material variant with identical chemical composition $\sim \text{Fe}_{32}\text{Co}_{28}\text{Ni}_{28}\text{Ta}_5\text{Al}_7$ (at.%) but smaller particle size (S-MCA, annealed for 1 h, producing an average particle size of $\sim 24 \pm 15$ nm), larger particle size (L-MCA, annealed for 100 h, average particle size of $\sim 255 \pm 49$ nm) and the particle-free $\text{Fe}_{35}\text{Co}_{30}\text{Ni}_{30}\text{Ta}_5$ (at.%) alloy⁹, are also presented in Fig. 2a.

Compared with the single-phase $\text{Fe}_{35}\text{Co}_{30}\text{Ni}_{30}\text{Ta}_5$ (at.%) alloy with a relatively low value of σ_y of ~ 501 MPa, the notable increase in yield strength ($\sigma_y \sim 904$ MPa) of the M-MCA can be attributed to the precipitation strengthening of the L₁₂ particles with a high volume fraction ($\sim 55\%$). More importantly, such improvement in the strength of the M-MCA is achieved at no expense of ductility, which is fundamentally different from the case of the S-MCA where a significant loss in ductility is observed with increasing strength. The good ductility is correlated with the high work-hardening capability, as shown in Fig. 2b. Further increase of particle size at longer annealing time (100 h) in the L-MCA leads to the decrease of ductility (53%) and ultimate tensile strength (14%) as compared to those of the M-MCA. This is related to the mechanical weakness, strain localization

and embrittlement in the particle-free zone adjacent to the grain boundary caused by solute depletion (Extended Data Fig. 2a). This interfacial weakening has been confirmed by the associated fracture morphologies, with typical ductile fracture with fine dimples in the M-MCA material (see Fig. 2b inset) and intergranular fracture in the L-MCA material (Extended Data Fig. 2b).

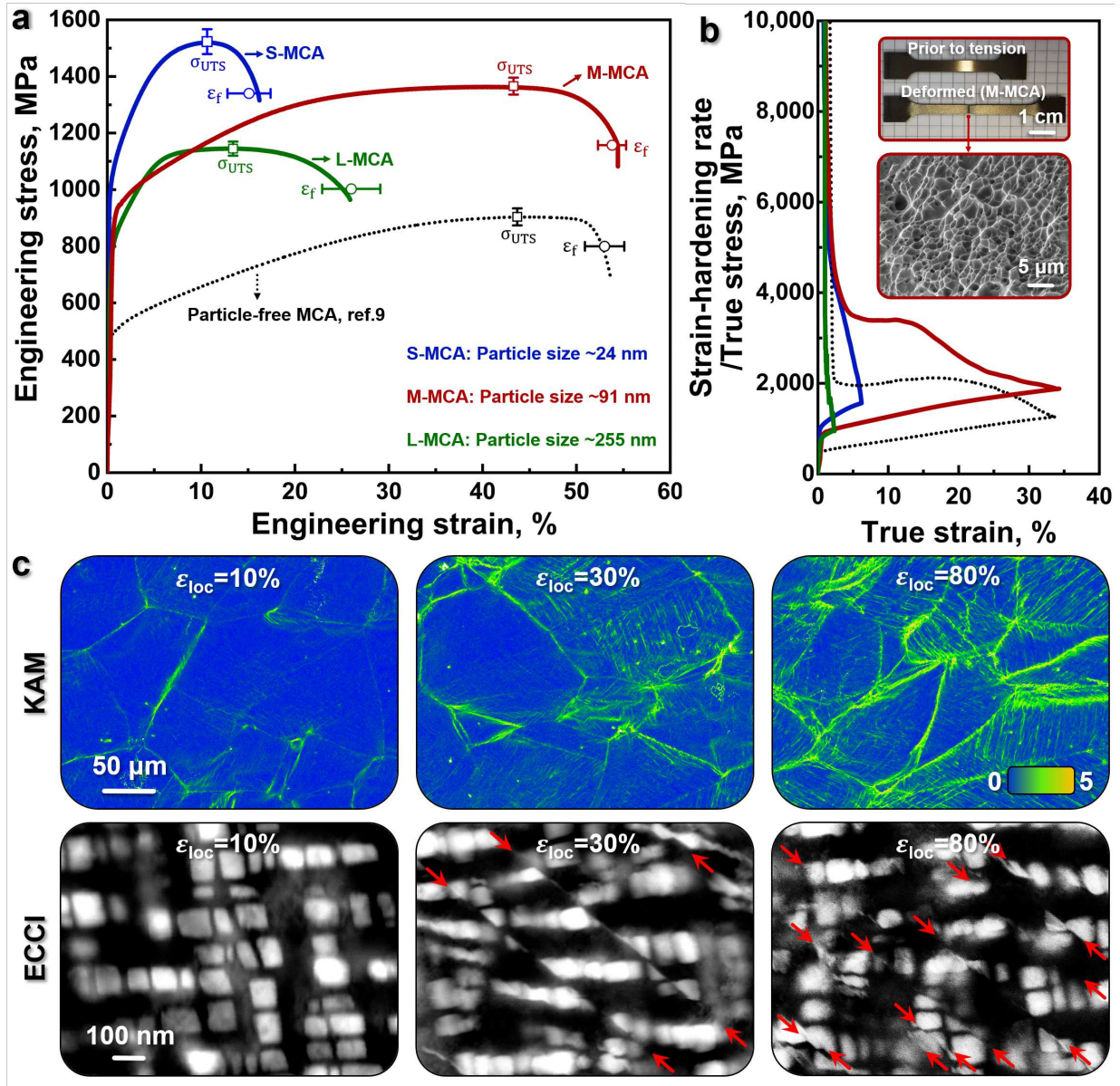


Figure 2 | Mechanical behaviour and nanoscale processes during plastic straining of the M-MCA. a, Typical engineering stress-strain curves measured at room-temperature together with the average value for ultimate tensile strength (σ_{UTS}) and elongation at fracture (ϵ_f). **b,** Strain

hardening rate/true stress–true strain curves. The insets show the macroscopic image (upper inset) of the tensile sample and corresponding fracture morphology (bottom inset), typical ductile fracture with fine dimple structures is observed. **c**, Substructure evolution as a function of deformation: EBSD–KAM maps revealing the deformation-induced strain distribution (upper); ECCI analysis (bottom) showing the evolution of microbands, and the shearing of L1₂ particles are highlighted by red arrows.

To unravel the mechanisms responsible for the significant improvement in the strength-ductility combination of the M-MCA, we investigated its deformation substructures using EBSD kernel average misorientation (KAM) analysis and ECCI at different hardening stages (Fig. 2c). The underlying processes are summarized in the schematics in the Extended Data Fig. 3. In principle, high strength requires to impede dislocation movement while good ductility needs mobility of dislocations and new production of dislocations²⁰. At the early deformation stage (local strain, ε_{loc} =10%), M-MCA deforms by planar dislocation glide on {111} planes (Extended Data Fig. 4a), as commonly observed in fcc alloys²¹. The dislocations extend through the grains. Corresponding pile-up configurations at the grain boundaries are revealed by the higher KAM values (Fig. 2c). The relatively large grain size (~85 μ m) of the current M-MCA enables higher mobility of dislocations compared to most of the previously reported strong MCAs that had smaller grain size²²⁻²⁴ (~10 μ m). Further straining (ε_{loc} =30%) refines the crystallographically aligned microbands (Extended Data Fig. 4b). The refinement facilitates the shearing of L1₂ particles (see ECC images in Fig. 2c). A further refined and curved microband structure is observed at high local strains ε_{loc} of ~80% (Extended Data Fig. 4c). The quantification of the evolution of the average microband spacing reveals a microband refinement process during straining (Extended Data Fig. 4d). The gradually reduced microband spacing causes a higher passing stress and thus enhanced strain hardening. This has been proposed to explain the good strength-ductility combinations in some high manganese steels²⁵⁻²⁷ and MCAs²⁸. Hence, the observed dynamic microband refinement and particle shearing are the prevalent deformation mechanisms in the current MCAs. No Orowan looping was observed, even when increasing the average particle size up to 255 nm for the L-MCA (Extended Data Fig. 2c), as the average particle spacing (Extended Data Table 1) remains far below the critical value (~3094 nm, see Extended Data for detailed calculation) for the activation of dislocation bowing around particles, a mechanism referred to as Orowan effect. Furthermore, the

stress required for shearing particles in the M-MCA with a medium particle size ($\sim 91 \pm 36$ nm) with high volume fraction ($\sim 55\%$) is 2.2 times larger than that for the S-MCA with a smaller particle size ($\sim 24 \pm 15$ nm) with low volume fraction (43%) (see Extended Data for detailed calculation). Therefore, the high critical shear stress required for cutting the L_{12} particles and the dynamic microband refinement during plastic deformation lead to the strong strain hardening capacity of the M-MCA.

Fig. 3a and b show the magnetic properties of the MCAs. All alloys exhibit typical soft ferromagnetic behaviour. The M-MCA shows an optimal combination of an extremely low coercivity of ~ 78 A/m (< 1 Oe) and a saturation magnetization (M_s) of ~ 100 Am²/kg. We identified a higher M_s for the alloy variant with larger average particle size (see inset in Fig. 3a). The reason behind this is the change in intrinsic magnetic behaviour, as indicated by the higher Curie temperature (T_c), revealed by the thermomagnetic curves (Extended Data Fig. 5a). Two distinct changes of the slope, indicating two ferromagnetic phases, are observed in the S-MCA. In contrast, only one sharp drop is observed in the M-MCA and L-MCA materials, indicating only one ferromagnetic phase. This is further confirmed by measuring the magnetic behaviour of the MCAs at elevated-temperature (Extended Data Fig. 5b). Considering that both, the fcc and L_{12} phases contain high concentrations of ferromagnetic elements, we investigated their individual magnetic response through casting both phases as separate bulk samples with their respective nominal compositions acquired before from APT analysis (see Methods for details). The results reveal that the L_{12} bulk phase is paramagnetic while the fcc matrix is ferromagnetic in the M-MCA (Extended Data Fig. 5c). Due to different partitioning, the magnetic behaviour of the L_{12} phase varies from ferromagnetic in the S-MCA material variant to paramagnetic in the M-MCA and L-MCA materials. The mechanism behind this transition is the change in the intrinsic spin alignment, which is related to the change in chemical composition (Extended Data Figure 6) and ordering during annealing. The overall increase in saturation magnetization of the MCAs as a function of particle coarsening is attributed to the change in fcc matrix composition due to elemental partitioning (Extended Data Fig. 6), i.e., specifically to the resultant higher concentration of (Fe+Co) in the fcc matrix. This effect enhances the total average magnetic moment per formula unit and leads to higher a M_s .

To gain further insight into the mechanism behind the magnetic response of the M-MCA, we investigated the magnetic domain structure in terms of magneto-optical Kerr effect (MOKE) microscopy (Fig. 3c) under different applied magnetic field strengths. Starting from the alternating current (AC) demagnetized state to an applied field of 40 kA/m, the nucleation of magnetic domains is uniformly distributed within the grain. Further increasing the applied field (~155 kA/m) leads to domain wall movement and growth of the energetically favourable domains. The domains grow smoothly within the grains while the movement is hindered at the grain/twin boundaries (Extended Data Fig. 7). Fig. 3d summarized the statistically averaged particle size distribution with respect to the coercivity of all the MCA samples at different annealed states. The data is acquired by developing an automated processing protocol, as shown in Extended Data Fig. 8. The coercivity first decreases from 763 A/m (S-MCA, average particle size ~24 nm) to 78 A/m (M-MCA, average particle size ~91 nm) and then increases to 1745 A/m (L-MCA, average particle size ~255 nm). Both the average particle size and the grain size increase monotonously with increasing annealing time (Extended Data Table 1). Since the grain size of the MCAs material is above the critical single-domain size, its coercivity decreases with grain coarsening, following the model for the grain size dependence of the coercivity as $H_c \propto 1/D$ (where D is the grain size)¹¹. However, the magnitude of the decrease in coercivity due to grain coarsening according to the model is negligible compared to the experimentally observed values: The difference according to the model calculation between the S-MCA and M-MCA material variants is ~2 A/m, yet, the experimentally observed difference is ~775 A/m. Accordingly, the energy required for the irreversible displacement of domain walls within the grain is the determining effect for the extremely low coercivity.

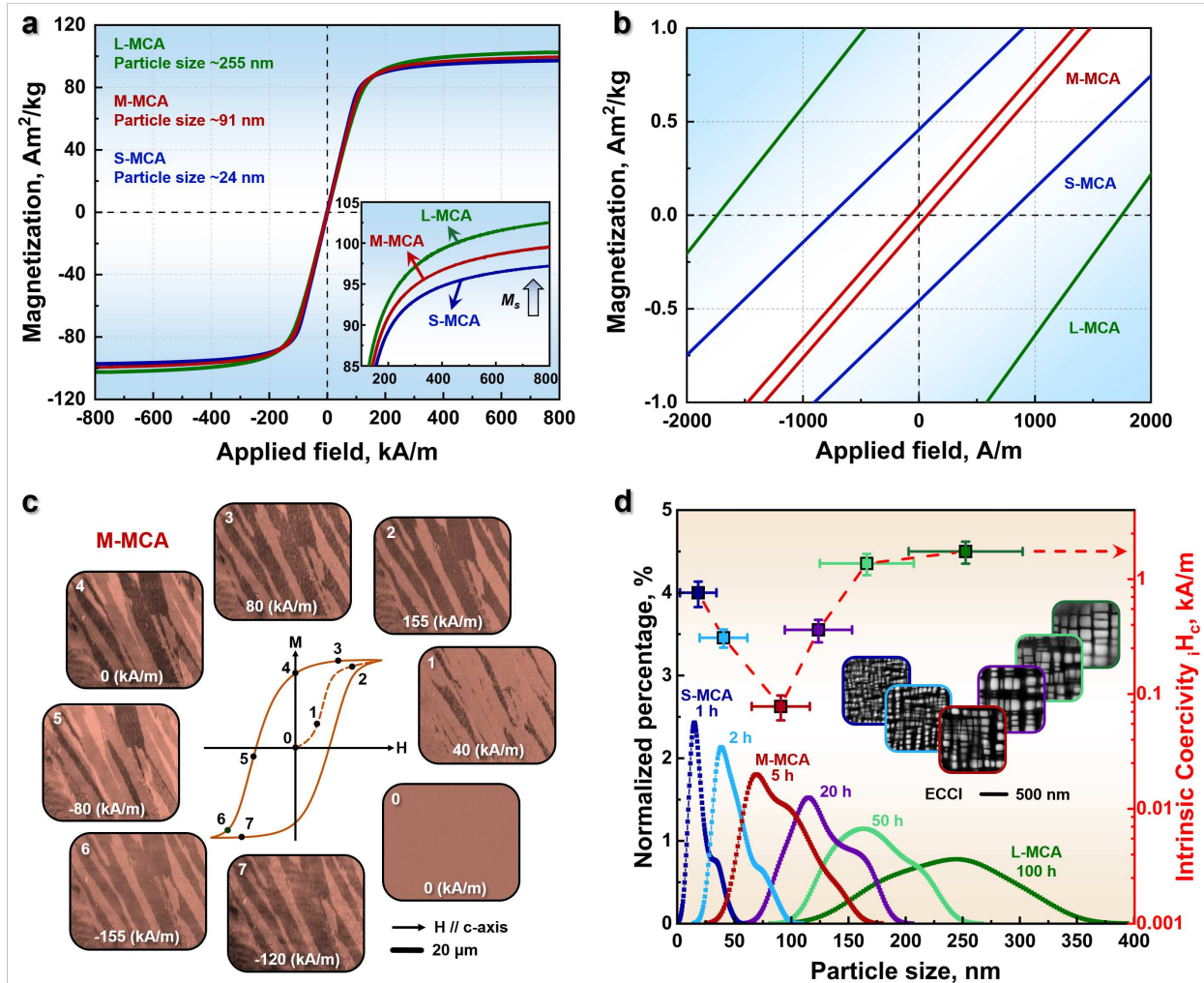


Figure 3 | Soft magnetic response and associated Bloch wall motion behaviour of the MCAs at room-temperature. **a**, Hysteresis loops (M/H) acquired up to ± 800 kA/m. The magnetic field-sweeping rate is 1 kA/m. The inset shows the enlarged view of the increase in saturation magnetization with particle coarsening. **b**, M/H curves measured at a rate of 0.1 kA/m between ± 50 kA/m, showing the extremely low coercivity. **c**, MOKE microscopy observation, in longitudinal contrast, revealing the magnetization process. The applied magnetic field is horizontal to the viewing plane. **d**, Statistical particle size distribution of all the MCAs under different isothermal heat treatment conditions (1~100 h at 1173 K). The right inset shows the evolution of particle size by ECCI probing.

Therefore, the significant drop in coercivity at the early particle coarsening stage (≤ 91 nm) is attributed to the gradual reduction of the overall coherency stresses between matrix and particles, due to their average size increase (see Extended Data for further calculation details). More specific, the values of the specific surface area \times integrated lattice misfit decrease from 1.09×10^6 m⁻¹ in the S-MCA material to 4.08×10^5 m⁻¹ in the M-MCA material. The dislocation density in the matrix decreases from 1.50×10^{14} m⁻² in the S-MCA material to 9.32×10^{13} m⁻² in the M-MCA material when increasing the annealing time from 1 h to 5 h (see Extended Data for the dislocation density calculation). The reduction in dislocation density lowers the elastic distortion fields that can pin the domain walls. Although the elastic distortion and dislocation density decrease with particle coarsening, the coercivity of the L-MCA material increases. Two main mechanisms are proposed to explain this. First, the average particle size and the associated strain field in the L-MCA becomes larger than the domain wall width (δ_w), leading to domain wall pinning. The L-MCA has a δ_w of ~ 117 nm and a much larger average particle size of ~ 255 nm, whereas the average particle size of the M-MCA is ~ 91 nm, which is below its δ_w of ~ 112 nm (see Extended Data for the estimation of the domain wall width). Second, the increased magnetostatic energy (E_s) associated with the paramagnetic particles causes a stronger individual pinning effect of each particle on the domain wall motion. More specifically, the E_s of the L-MCA is estimated to be 23 times larger than that of the M-MCA (see Extended Data for calculation details). When only considering particle size, it should be noted that for the M-MCA, the coherent particles distributed along the grain boundaries with an average size (~ 160 nm) above the δ_w (~ 112 nm) are expected to have a stronger pinning effect on the domain walls than those in the grain interiors (~ 91 nm). However, these coarser particles only occupy a small fraction ($\sim 1.2\%$ in M-MCA), hence, with a negligible effect on domain wall motion.

These considerations show that the nanoscale size distribution of the particles must be carefully controlled to minimize their pinning effect on domain wall movement, which determines the alloy's coercivity. This is achieved here by an optimal balance between the release of structural defects (e.g., interfacial elastic distortion, dislocation density) just down to a level required to maintain high mechanical strength and the rise of the pinning effect from the magnetostatic energy, while keeping the particle size below the domain wall width during particle coarsening.

To highlight the pronounced combination of mechanical and soft magnetic properties of the M-MCA with optimal particle size, we compare it with existing soft magnetic materials in an Ashby-plot showing the ultimate tensile strength (σ_{UTS}) \times elongation at fracture (ϵ_f) against the intrinsic coercivity, Fig. 4a. This comparison shows that the $\sigma_{UTS}\times\epsilon_f$ value of the new M-MCA material outperforms all other soft magnetic materials. More importantly, the coercivity of the new material is lower than that of all NiFe alloys and other MCAs, comparable only to Fe-Si, CoFe alloys and pure Fe. A similar plot showing the $\sigma_{UTS}\times\epsilon_f$ values against the saturation induction is shown in the Extended Data Fig. 9. The comparison shows that the newly developed material with its extremely low coercivity has also a good saturation induction compared to other soft magnetic materials. Fig. 4b compares the $\sigma_{UTS}\times\epsilon_f$ value versus grain size of the M-MCA material with recently reported strong and ductile MCAs. The analysis shows that the current alloy reaches high values of $\sigma_{UTS}\times\epsilon_f$ even without the substantial contribution from grain boundary strengthening, confirming the significant strengthening provided by the nanoparticles and the massive solid solution matrix in the current MCA.

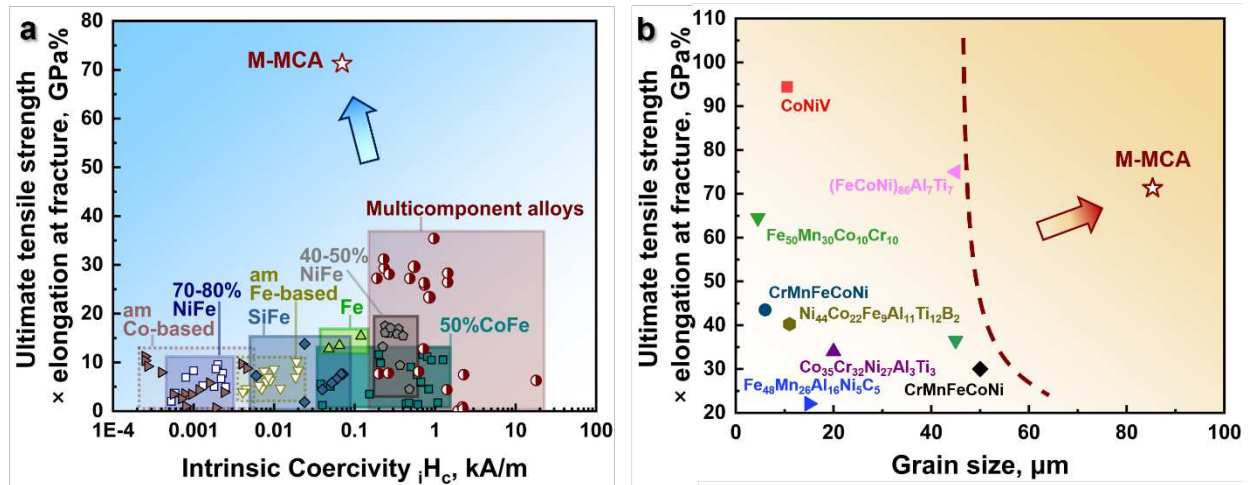


Figure 4 | Mechanical and magnetic features combined in the new Fe₃₂Co₂₈Ni₂₈Ta₅Al₇ (at.%) M-MCA material. **a**, Ashby map compiling room-temperature ultimate tensile strength (σ_{UTS}) \times elongation at fracture (ϵ_f) and intrinsic coercivity compared to those of other soft magnetic materials, such as NiFe^{29,30}, CoFe^{31,32}, SiFe³³, Fe³⁴, amorphous alloys^{4,35-37} and established MCAs³⁸⁻⁴⁹. **b**, Ashby map showing $\sigma_{UTS}\times\epsilon_f$ versus average grain size compared to those of other strong and ductile MCAs^{22-24,50-53}. ‘am’ in the legend stands for amorphous alloys.

Here we have developed a new material which unifies so far mutually exclusive properties, namely, high mechanical strength (1336 MPa), high tensile ductility (54%), extremely low coercivity (78 A/m) and good saturation magnetization (100 Am²/kg). We realized this in a new class of bulk SMMs through a nanoparticle dispersion with well-controlled size (~91 nm), magnetic properties, coherency strain, strength and interface energy. The design strategy is opposite to that generally applied in conventional SMM design. Instead of using smallest microstructure features (particle size <15 nm) to avoid magnetic wall pinning as in conventional SMMs, we have chosen a relatively coarse particle dispersion with tuned particle/matrix interfacial coherency stresses and paramagnetic properties to minimize magnetic pinning of domain walls on the one hand (soft magnetism) and maximize interaction strength with dislocations on the other hand (strength and ductility). Such a particle design concept can be applied also to many other precipitation-containing soft magnetic alloys, suited to serve in a broad spectrum of mechanically-demanding energy, automotive and aerospace applications.

References

- 1 J. M. Silveyra, *et al. Science* **362**, eaao0195 (2018). <https://doi.org/10.1126/science.aao0195>
- 2 S. Velayos, V. Sanchez-Giron, *Nature* **157**, 583 (1946). <https://doi.org/10.1038/157583b0>
- 3 O. Gutfleisch, *et al. Adv. Mater.* **23**, 821–842 (2011). <https://doi.org/10.1002/adma.201002180>
- 4 A. Inoue, *et al. Nat. Mater.* **2**, 661–663 (2003). <https://doi.org/10.1038/nmat982>
- 5 T. Hasegawa, *et al. Sci. Rep.* **7**, 13125 (2017). <https://doi.org/10.1038/s41598-017-13602-x>
- 6 B. D. Cullity, C. D. Graham, *Introduction to Magnetic Materials* (IEEE Press, ed. 2nd, 2009). <https://doi.org/10.1002/9780470386323>
- 7 G. Herzer, *IEEE Trans. Magn.* **26**, 1397–1402 (1990). <https://doi.org/10.1109/20.104389>
- 8 Y. Ma, *et al. Adv. Mater.* **33**, 2006723 (2021). <https://doi.org/10.1002/adma.202006723>
- 9 L. Han, *et al. Adv. Mater.* **33**, 2102139 (2021). <https://doi.org/10.1002/adma.202102139>
- 10 Z. Fu, *et al. Appl. Mater. Today*, **15**, 590–598 (2019). <https://doi.org/10.1016/j.apmt.2019.04.014>
- 11 G. Herzer, *IEEE Trans. Magn.* **25**, 3327–3329 (1989). <https://doi.org/10.1109/20.42292>
- 12 T. Osaka, *et al. Nature* **392**, 796–798 (1998). <https://doi.org/10.1038/33888>
- 13 L. Landau, E. Lifshitz, *Phys. Z.* **8**, 153–164 (1935). <https://doi.org/10.1016/B978-0-08-036364-6.50008-9>
- 14 L. Néel, *Cah. Phys.* **25**, 1–20 (1944).
- 15 S. Chikazumi, C. D. Graham, *Physics of Ferromagnetism*. (Oxford University, 2012). ISBN: 978-3-642-25582-3
- 16 A. G. Khachaturyan, *Theory of Structural Transformations in Solids* (Courier Corporation, 2013). ISBN: 978-0-486-46280-6
- 17 R. J. Hill, C. J. Howard, *J. Appl. Cryst.* **20**, 467–474 (1987). <https://doi.org/10.1107/S0021889887086199>
- 18 S. Jiang, *et al. Nature* **544**, 460–464 (2017). <https://doi.org/10.1038/nature22032>
- 19 T. Yang, *et al. Science* **362**, 933–937 (2018). <https://doi.org/10.1126/science.aas8815>
- 20 S. Tolansky, *Nature* **209**, 1058–1059 (1966). <https://doi.org/10.1038/2091058b0>
- 21 C. S. Pande, P. M. Hazzledine, *Philos. Mag.* **24**, 1393–1410 (1971).
- 22 T. Yang, *et al. Science* **369**, 427–432 (2020). <https://doi.org/10.1126/science.abb6830>
- 23 H. Luo, *et al. Nat Commun* **11**, 3081 (2020). <https://doi.org/10.1038/s41467-020-16791-8>
- 24 Z. Wang, *et al. Sci. Adv.* **6**, eaba9543 (2020). <https://doi.org/doi:10.1126/sciadv.aba9543>
- 25 E. Welsch, *et al. Acta Mater.* **116**, 188–199 (2016). <https://doi.org/10.1016/j.actamat.2016.06.037>
- 26 M. Yao, *et al. Acta Mater.* **140**, 258–273 (2017). <https://doi.org/10.1016/j.actamat.2017.08.049>
- 27 Z. Wang, *et al. Acta Mater.* **198**, 258–270 (2020). <https://doi.org/10.1016/j.actamat.2020.08.003>
- 28 Z. Wang, *et al. Acta Mater.* **126**, 346–360 (2017). <https://doi.org/10.1016/j.actamat.2016.12.074>
- 29 T. R. Christenson, *et al. MRS Online Proc. Libr.* **518**, 185–190 (1998). <https://doi.org/10.1557/PR-OC-518-185>
- 30 P. V. Yekta, *et al. J. Magn. Magn. Mater.* **468**, 155–163 (2018). <https://doi.org/10.1016/j.jmmm.2018.07.088>
- 31 E. P. George, *et al. Mater. Sci. Eng., A* **329**, 325–333 (2002). [https://doi.org/10.1016/S0921-5093\(01\)01594-5](https://doi.org/10.1016/S0921-5093(01)01594-5)
- 32 R. M. Bozorth, *Ferromagnetism*. (Wiley, 1993). ISBN: 978-0-780-31032-2
- 33 C. W. Chen, *Magnetism and metallurgy of soft magnetic materials* (Courier Corporation, 2013). ISBN-0-486-64997-0
- 34 W. Pepperhoff, M. Acet, *Constitution and Magnetism of Iron and its Alloys*. (Springer, 2013). ISBN 978-3-662-04345-5
- 35 A. Inoue, *et al. Acta Mater.* **52**, 1631–1637 (2004). <https://doi.org/10.1016/j.actamat.2003.12.008>
- 36 C. Y. Lin, *et al. J. Phys. D: Appl. Phys.* **40**, 310–314 (2007). <https://doi.org/10.1088/0022-3727/40/2/004>
- 37 B. Shen, *et al. Appl. Phys. Lett.* **85**, 4911–4913 (2004). <https://doi.org/10.1063/1.1827349>

- 38 Y. Zhang, *et al. Sci Rep* **3**, 1455 (2013). <https://doi.org/10.1038/srep01455>
- 39 F. Körmann, *et al. Appl. Phys. Lett.* **107**, 142404 (2015). <https://doi.org/10.1063/1.4932571>
- 40 P. Li, *et al. J. Alloys Compd.* **694**, 55–60 (2017). <https://doi.org/10.1016/j.jallcom.2016.09.186>
- 41 T. T. Zuo, *et al. J. Magn. Magn. Mater.* **371**, 60–68 (2014). <https://doi.org/10.1016/j.jmmm.2014.07.023>
- 42 Y. P. Wang, *et al. Adv. Eng. Mater.* **11**, 641–644 (2009). <https://doi.org/10.1002/adem.200900057>
- 43 K. B. Zhang, *et al. J. Alloys Compd.* **502**, 295–299, (2010). <https://doi.org/10.1016/j.jallcom.2009.11.104>
- 44 S. G. Ma, Y. Zhang, *Mater. Sci. Eng., A* **532**, 480–486 (2012). <https://doi.org/10.1016/j.msea.2011.10.110>
- 45 K. Zhang, Z. Fu, *Intermetallics* **28**, 34–39 (2012). <https://doi.org/10.1016/j.intermet.2012.03.059>
- 46 S. M. Na, *et al. AIP Advances* **8**, 056412 (2018). <https://doi.org/10.1063/1.5007073>
- 47 H. Duan, *et al. Mater. Res. Bull.* **111**, 289–293 (2019). <https://doi.org/10.1016/j.materresbull.2018.11.036>
- 48 H. Zhang, *et al. J. Magn. Magn. Mater.* **478**, 116–121 (2019). <https://doi.org/10.1016/j.jmmm.2019.01.096>
- 49 T. Zuo, *et al. Intermetallics* **100**, 1–8 (2018). <https://doi.org/10.1016/j.intermet.2018.05.014>
- 50 Z. Li, *et al. Nature* **534**, 227–230 (2016). <https://doi.org/10.1038/nature17981>
- 51 X. H. Du, *et al. Nat Commun* **11**, 2390 (2020). <https://doi.org/10.1038/s41467-020-16085-z>
- 52 B. Gludovatz, *et al. Science* **345**, 1153–1158 (2014). <https://doi.org/10.1126/science.1254581>
- 53 Z. Wu, *et al. Acta Mater.* **81**, 428–441 (2014). <https://doi.org/10.1016/j.actamat.2014.08.026>

Methods

Materials preparation. The bulk MCA ingot with a predetermined nominal composition of $\text{Co}_{27.7}\text{Fe}_{32.6}\text{Ni}_{27.7}\text{Ta}_{5.0}\text{Al}_{7.0}$ (at%) was first cast in a vacuum induction furnace using pure metallic ingredients (purity higher than 99.8 wt.%) under high-purity argon (Ar) atmosphere. The as-cast ingot with a dimension of 40 mm×60 mm×20 mm (*length*×*width*×*thickness*) was then hot-rolled at 1473 K to an engineering thickness reduction of 50% (final thickness ~10 mm). After hot-rolling, The alloy sheets were then homogenized at 1473 K for 10 min in Ar atmosphere followed by water-quenching. To obtain a wide size distribution of the particles, further isothermal heat treatments were conducted at 1173 K, lasting from 1 h up to 100 h (1 h, 2 h, 5 h, 20 h, 50 h, 100 h) in Ar atmosphere and followed by water quenching. The exact chemical composition of the MCA measured by wet-chemical analysis is $\text{Co}_{28.0}\text{Fe}_{32.0}\text{Ni}_{28.1}\text{Ta}_{4.7}\text{Al}_{7.2}$ (at.%), which is close to the pre-designed composition. In addition, the bulk ingots (~50 g) with the compositions identical to that of the fcc ($\text{Fe}_{36}\text{Co}_{28}\text{Ni}_{26}\text{Al}_7\text{Ta}_3$, at%) matrix phase and the L1_2 particle ($\text{Ni}_{40}\text{Co}_{26}\text{Ta}_{13}\text{Fe}_{12}\text{Al}_9$, at%) in the M-MCA derived from the APT analysis were also cast, respectively, by arc-melting under Ar atmosphere. The ingots were remelted six times to achieve chemical homogeneity.

Analytical methods. X-ray diffraction (XRD) measurements were carried out in an X-ray system (Diffractometer D8 Advance A25-X1) with Co K α radiation ($\lambda=1.78897\text{\AA}$, 35 kV and 40 mA). Electron backscatter diffraction (EBSD) characterizations were conducted in a Zeiss-Crossbeam focus ion beam scanning electron microscope at 15 kV. Electron channelling contrast imaging (ECCI) characterizations were performed using a Zeiss-Merlin high-resolution field emission electron microscope at 30 kV. Transmission electron microscopy (TEM) analysis including selected area electron diffraction (SAED) was conducted in a JEOL JEM 2100 at 200 kV. Scanning transmission electron microscopy (STEM) images were collected using a probe-corrected Titan Themis 60-300 (Thermo Fischer Scientific) microscope. To modify the Z-contrast characteristics of the imaging mode, high-angle annular dark-field (HAADF) micrographs with a convergence angle of 23.8 mrad were acquired at 300 kV. The resulting collection angle ranges from 73 mrad to 200 mrad. Further energy-dispersive X-ray spectroscopy (EDS) analysis was conducted using Thermo Fischer Scientific's Super-X windowless EDS detector at an acceleration voltage of 300 kV. Atom probe tomography (APT) experiments were performed in a local electrode atom probe (LEAP 5000 XR) from Cameca Instruments Inc and analyzed with commercial AP Suite software (v 6.1). A pulse frequency of ~ 125 kHz, a pulse energy of ~ 40 pJ, and a temperature of ~ 60 K was used. The detection rate was kept at a frequency of 1 ion per 100 pulses.

Mechanical response measurements. Room-temperature uniaxial tensile tests were performed using flat tensile specimens at an initial strain rate of $1 \times 10^{-3} \text{ s}^{-1}$. The tensile specimens in two-gauge dimensions were machined along the rolling direction from the alloy sheets by electrical discharge machining. The specimens with a total length of 60 mm, a gauge length of 30 mm, a gauge width of 5 mm and a thickness of 2 mm were used to probe the bulk tensile properties. Further, smaller tensile specimens with a total length of 20 mm, a gauge length of 10 mm, a gauge width of 2 mm and a thickness of 1 mm were used to measure the local strain evolution by the digital image correlation (DIC) method. At least four specimens for each condition were tested to confirm reproducibility.

Magnetic response measurements. The magnetic response was evaluated using the Quantum Design Magnetic Properties Measurement System (MPMS) equipped with a standard vibrating sample magnetometry (VSM) option. Cuboid specimens in $\sim 3 \text{ mm} \times 3 \text{ mm} \times 1 \text{ mm}$ (*length* \times *width* \times *thickness*) were used for the measurements. The hysteresis loops $M(H)$ were

performed in an external magnetic field of ± 800 kA/m at a magnetic field-sweeping rate of 1 kA/m at 10 K, 300 K, 500 K and 800 K, respectively. The temperature dependence of magnetization $M(T)$ analysis was carried out under an applied field of 40 kA/m from 10 K to 1000 K with a temperature-sweeping rate of 10 K/min.

The magnetic domain patterns were characterized by a magneto-optical Kerr effect (MOKE) Zeiss microscope (Axio Imager.D2m). The domain wall movement was captured under an applied magnetic field of ± 155 kA/m. Prior to the measurement, a background image was collected as a reference in the alternating current (AC) demagnetized state. The images acquired at different applied fields were enhanced by subtracting the background image using KerrLab software.

Estimation of interfacial coherency stress

The coherency stress at the $L1_2/fcc$ interface is determined by integrating the lattice misfit across the interface as:

$$\delta = S_{L1_2/fcc} \sum \delta_x$$

where $S_{L1_2/fcc}$ is the $L1_2/fcc$ interface area related to the average particle size (d), the volume fraction of the $L1_2$ particles (f) and the overall volume (V) as follows:

$$S_{L1_2/fcc} = \frac{Vf}{4/3\pi \cdot (\frac{d}{2})^3} 4\pi(d/2)^2 = \frac{6Vf}{d}$$

δ_x is the varying lattice misfit as a function of distance (x) from the $L1_2/fcc$ interface determined by the following equation¹⁶:

$$\delta_x = 2 \times \left[\frac{a_x^{L1_2} - a_x^{fcc}}{a_x^{L1_2} + a_x^{fcc}} \right]$$

$a_x^{L1_2}$ and a_x^{fcc} are the lattice parameters of the $L1_2$ and fcc phases at the interfacial region. Such values were calculated using the $L1_2/fcc$ interfacial chemical compositions acquired from the APT datasets with Vegard's relation⁵⁴:

$$a_x^{L1_2} = a_0^{L1_2} + \sum_i \Gamma_i^{L1_2} x_i^{L1_2}$$

$$a_x^{fcc} = a_0^{fcc} + \sum_i \Gamma_i^{fcc} x_i^{fcc}$$

where $a_0^{L1_2}$ and a_0^{fcc} are the average lattice parameters for the $L1_2$ particles and the fcc matrix, respectively, derived from the Rietveld simulation based on the XRD measurements, as shown in Extended Data Table 1. $\Gamma_i^{L1_2}$ and Γ_i^{fcc} are the Vegard coefficients for the $L1_2$ and fcc phases obtained from the ordered Ni_3Al phase and disordered fcc phase in the Ni-base superalloys⁵⁵, as shown in Extended Data Table 2. Note that the above-calculated lattice misfit δ_l represents the theoretical unconstrained state. This can be related to the constrained misfit (ε) by elasticity theory as below⁵⁶:

$$\varepsilon = \frac{3}{2} \delta_l$$

The estimated interfacial constrained misfit value is 1.09×10^6 , 4.08×10^5 and 1.96×10^5 for the S-MCA, M-MCA and L-MCA, respectively. Therefore, the significant decrease in the interfacial coherency stress is expected to play an essential role in releasing the pinning effect on domain wall movement with particle coarsening for the MCAs with the particle size below the domain wall width.

Estimation of dislocation density

The dislocation density (ρ) in the fcc matrix can be calculated through the Williamson-Smallman relationship as⁵⁷:

$$\rho = \frac{2\sqrt{3}(\varepsilon_s^2)^{1/2}}{Db}$$

where ε_s is microstrain, D is crystallite size acquired from the XRD profiles (Extended Data Table 1), and b is the Burgers vector (for fcc structure, $b = \sqrt{2}/2 \times a_{fcc}$)⁵⁸. The dislocation density in the fcc matrix is thus estimated to be $1.50 \times 10^{14} \text{ m}^{-2}$, $9.32 \times 10^{13} \text{ m}^{-2}$ and $5.38 \times 10^{13} \text{ m}^{-2}$ for the S-MCA, M-MCA and L-MCA, respectively. Based on the above estimation, the considerable improvement in the coercivity also derives from the decrease of dislocation density in the fcc matrix.

Estimation of particle shearing stress

Based on the experimental observation (Fig. 2c and Extended Data Fig. 2c), particle shearing is the primary deformation mechanism in the investigated MCAs. The strengthening contribution of particle shearing ($\Delta\tau$) is estimated according to⁵⁹:

$$\Delta\tau_{\text{Shearing}} = \frac{F}{b \cdot 2\lambda}$$

where 2λ is the mean spacing of the particles, $2\lambda \approx \sqrt{\frac{2}{f}}r$, r is the average radius of the particles ($r = d/2$). f is the volume fraction of the particles shown in Extended Data Table 1, F is the force exerted on the particles. The shearing strength is expressed as:

$$\Delta\tau_{\text{Shearing}} = k\sqrt{fr}$$

by using the relation $F \propto r^{3/2}$ and introducing constant k . The effect of particle strengthening of the M-MCA is then estimated to be two times larger than that of the S-MCA ($\Delta\tau_{M-MCA}/\Delta\tau_{S-MCA} = \frac{k\sqrt{f_{M-MCA} \cdot r_{M-MCA}}}{k\sqrt{f_{S-MCA} \cdot r_{S-MCA}}}$).

When considering the volume fraction of the particles to be constant, the mean spacing of the particles increases with increasing the particle size. As a result, the force required for shearing particles increases until the Orowan mechanism is activated, i.e., dislocations bowing the particles becomes easier than shearing. The critical mean spacing of the particles is determined by⁵⁹:

$$\Delta\tau_{\text{Shearing}} = \frac{F}{b \cdot 2\lambda} = \Delta\tau_{\text{Orowan}} = \frac{Gb}{2\lambda}$$

$G=84$ GPa is the adopted shear modulus⁶⁰. Consequently, the critical mean spacing of the particles is calculated as 3094.3 nm.

Estimation of magnetostatic energy

The magnetostatic energy (E_s) determines the coercive force which interacting between the paramagnetic particles (for M-MCA and L-MCA) and domain wall movement according to the formula³³:

$$E_s = \frac{1}{2} \mu_0 \frac{1}{3} M_s^2 \frac{4}{3} \pi r^3$$

where $\mu_0 = 4\pi \times 10^{-7}$ H/m is the permeability of vacuum, r is the average particle radius, M_s is the saturation magnetization of the fcc matrix. For M-MCA and L-MCA, in which the L1₂ phase is paramagnetic (Extended Data Fig. 5), the M_s of the fcc matrix is considered as the overall M_s of the alloy. The values of E_s significantly increase with increasing the particle size, that is, it varies from 6.5×10^{-24} (M-MCA) to 1.53×10^{-22} (L-MCA). The notable increase in magnetostatic energy results in a strong magnetic pinning effect.

Estimation of domain wall width

Strong pinning arises and results in the deterioration of coercivity when the microstructure defects have a comparable dimension to the domain wall thickness (δ_w). As a result, the estimation of the δ_w helps understand the ultralow coercivity in the current work is given by^{61,62}:

$$\delta_w = \pi(A_{ex}/K_1)^{1/2}$$

where $A_{ex} = k_B T_c / 2a_0$ is the exchange stiffness, $k_B = 1.380649 \times 10^{-23}$ J/K is the Boltzmann's constant, T_c and a_0 are the Curie temperature and lattice parameter of the fcc matrix, respectively (Extended Data Fig. 5d and Extended Data Table 1). K_1 is the first magnetocrystalline anisotropy constant. The value of K_1 (M-MCA) is taken from the Co-Fe system^{63,64} based on the composition of the fcc matrix (Fig. 1f) as 10.4 kJ/m³ (Al and Ta are non-ferromagnetic elements that do not show any magnetic moment, the chemical composition of the fcc phase $\sim \text{Fe}_{36}\text{Co}_{28}\text{Ni}_{26}\text{Al}_7\text{Ta}_3$, at.%, in the M-MCA is thus considered as $\sim \text{Co}_{31}(\text{Fe}+\text{Ni})_{69}$, at.%). The domain wall thickness of the M-MCA is thus estimated to be ~ 112 nm. Similarly, the domain wall thicknesses of the S-MCA and L-MCA are calculated as ~ 103 nm and 117 nm, respectively.

References

- 54 Y. Mishima, *et al. Acta Metall.* **33**, 1161–1169 (1985). [https://doi.org/10.1016/0001-6160\(85\)90211-1](https://doi.org/10.1016/0001-6160(85)90211-1)
- 55 H. Okamoto, *et al. Ni (Nickel) Binary Alloy Phase Diagrams* (ASM International, 1991) <https://doi.org/10.31399/asm.hb.v03.a0006189>
- 56 E. Nembach, G. Neite, *Prog. Mater. Sci.* **29**, 177–319 (1985). [https://doi.org/10.1016/0079-6425\(85\)90001-5](https://doi.org/10.1016/0079-6425(85)90001-5)
- 57 G. K. Williamson, W. H. Hall, *Acta Metall.* **1**, 22–31 (1953). [https://doi.org/10.1016/0001-6160\(53\)90006-6](https://doi.org/10.1016/0001-6160(53)90006-6)
- 58 W. D. Callister Jr, D. G. Rethwisch, *Fundamentals of materials science and engineering: an integrated approach*. (Wiley, 2018). ISBN: 978-1-119-17550-6
- 59 J. Roesler, *et al. Mechanical behaviour of engineering materials: metals, ceramics, polymers, and composites*. (Springer, 1st ed., New York, 2007).
- 60 Z. Wu, *et al. Acta Mater.* **81**, 428–441 (2014). <https://doi.org/10.1016/j.actamat.2014.08.026>
- 61 L. Néel, *Ann. Univ. Grenoble.* **22**, 299–343 (1946). http://www.numdam.org/item?id=AUG_1946__22_299_0
- 62 F. Pfeifer, C. Radloff, *J. Magn. Magn. Mater.* **19**, 190–207 (1980). [https://doi.org/10.1016/0304-8853\(80\)90592-2](https://doi.org/10.1016/0304-8853(80)90592-2)
- 63 L. W. McKeehan, *Phys. Rev.* **51**, 136–139 (1937). <https://doi.org/10.1103/PhysRev.51.136>
- 64 J. W. Shin, *Phys. Rev.* **46**, 139–142 (1934). <https://doi.org/10.1103/PhysRev.46.139>

Acknowledgements

The support of Prof. Gerhard Dehm at the Max-Planck-Institut für Eisenforschung is gratefully acknowledged. L. Han would like to acknowledge the financial support from the China Scholarship Council (201906370028). Z. Li. would like to acknowledge the National Natural Science Foundation of China (51971248) and the Hunan Special Funding for the Construction of Innovative Province (2019RS1001). O. Gutfleisch would like to acknowledge the Deutsche Forschungsgemeinschaft (405553726–TRR 270).

Author contributions

L. Han, Z. Li and D. Raabe designed the research project; L. Han, N. Peter and F. Maccari characterized the alloys; L. Han, I. Souza Filho, Y. Wei and B. Gault analyzed the data; L. Han, Z. Li, O. Gutfleisch and D. Raabe conceptualized the paper; all authors contributed to the discussion of the results.

Completing interests

The authors declare no competing interests.

Author Information

Reprints and permissions information is available at www.nature.com/reprints. The authors declare no competing financial interests. Readers are welcome to comment on the online version of the paper. Correspondence and requests for materials should be addressed to D. Raabe (d.raabe@mpie.de) or Z. Li (lizhiming@csu.edu.cn).

Figures

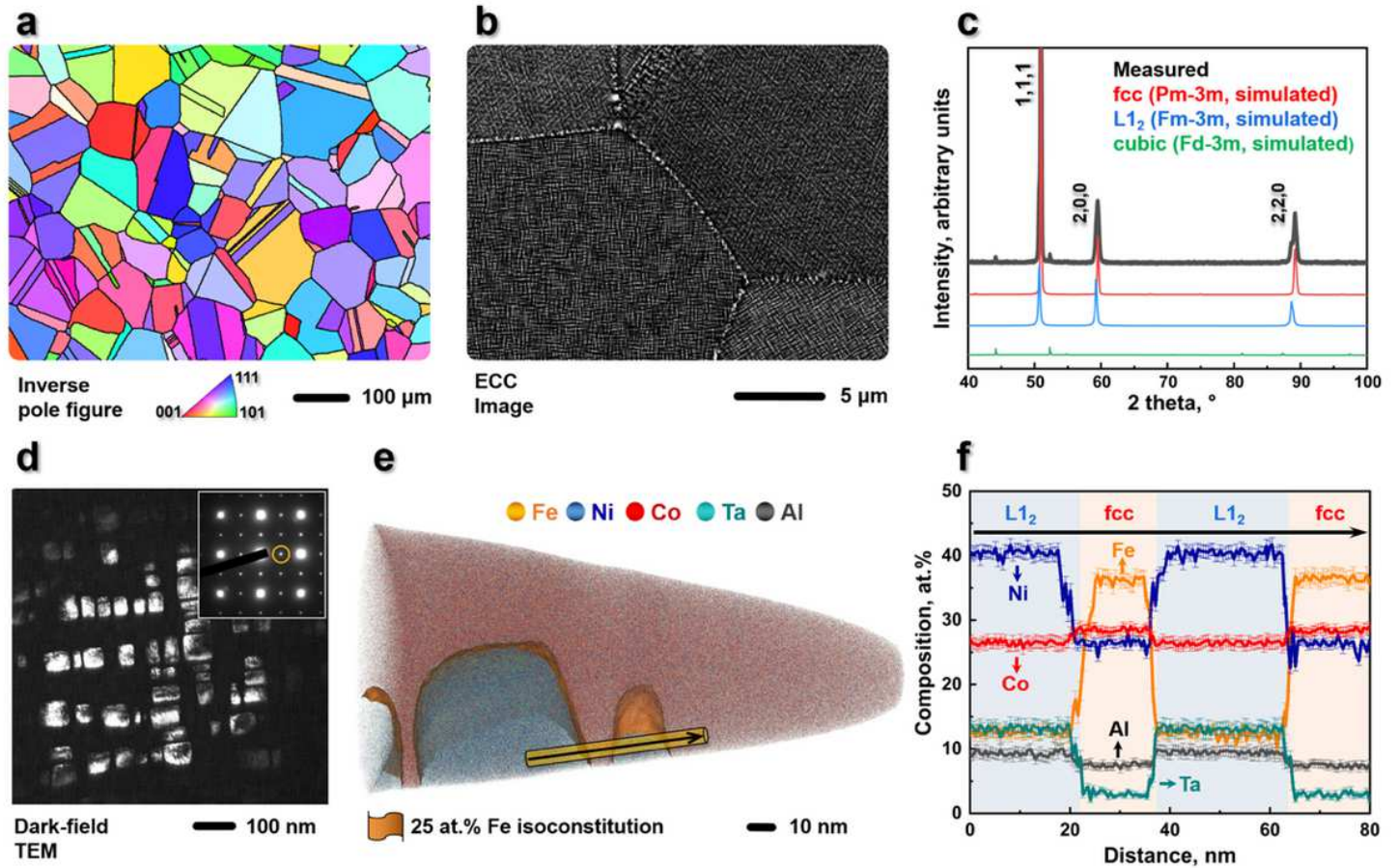


Figure 1

Microstructure and chemical composition of the M-MCA. a, EBSD-inverse pole figure (IPF) map showing the equiaxed grains of the fcc matrix. The black lines highlight the high-angle grain/twin boundaries. b, ECC image featuring the high-density uniformly distributed L1₂ particles in the grain interiors and heterogeneous particles at the grain boundaries. c, Measured and simulated XRD patterns showing the phase structures. d, Centered dark-field TEM image of the L1₂ particles obtained using the (011) superlattice spot (see inset). e, 3D reconstruction map of a typical APT tip showing the cuboidal L1₂ particles embedded in the fcc matrix. The L1₂/fcc interfaces are highlighted using iso-composition surfaces containing 25 at.% Fe. f, 1D compositional profiles computed along the cylinder region (marked by black arrow) in e, showing the compositional changes across several interfaces. Error bars refer to the standard deviations of the counting statistics in each bin of the profiles.

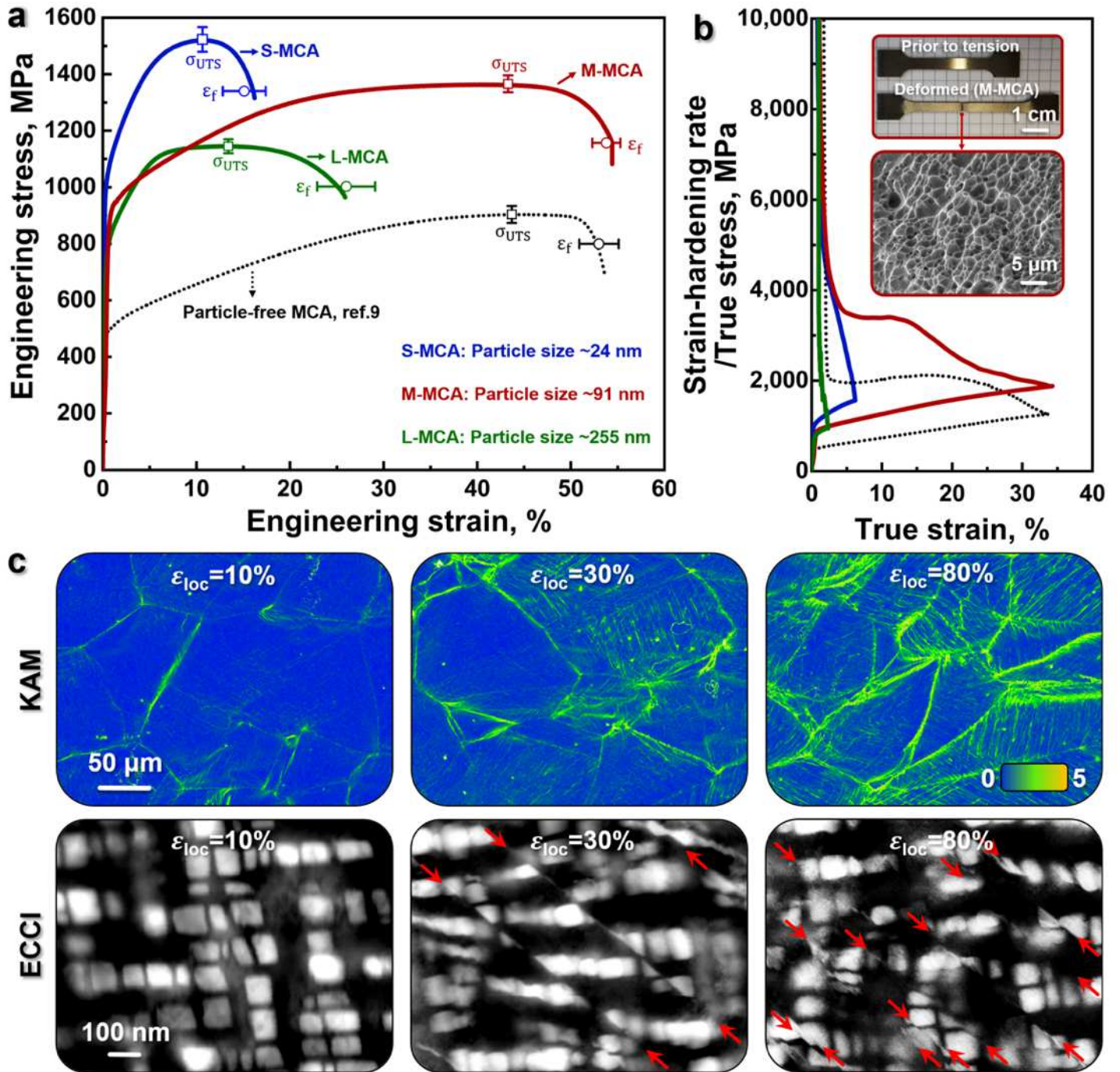


Figure 2

Mechanical behaviour and nanoscale processes during plastic straining of the M-MCA. a, Typical engineering stress-strain curves measured at room-temperature together with the average value for ultimate tensile strength (σ_{UTS}) and elongation at fracture (ϵ_f). b, Strain hardening rate/true stress-true strain curves. The insets show the macroscopic image (upper inset) of the tensile sample and corresponding fracture morphology (bottom inset), typical ductile fracture with fine dimple structures is observed. c, Substructure evolution as a function of deformation: EBSD-KAM maps revealing the deformation-induced strain distribution (upper); ECCI analysis (bottom) showing the evolution of microbands, and the shearing of L12 particles are highlighted by red arrows.

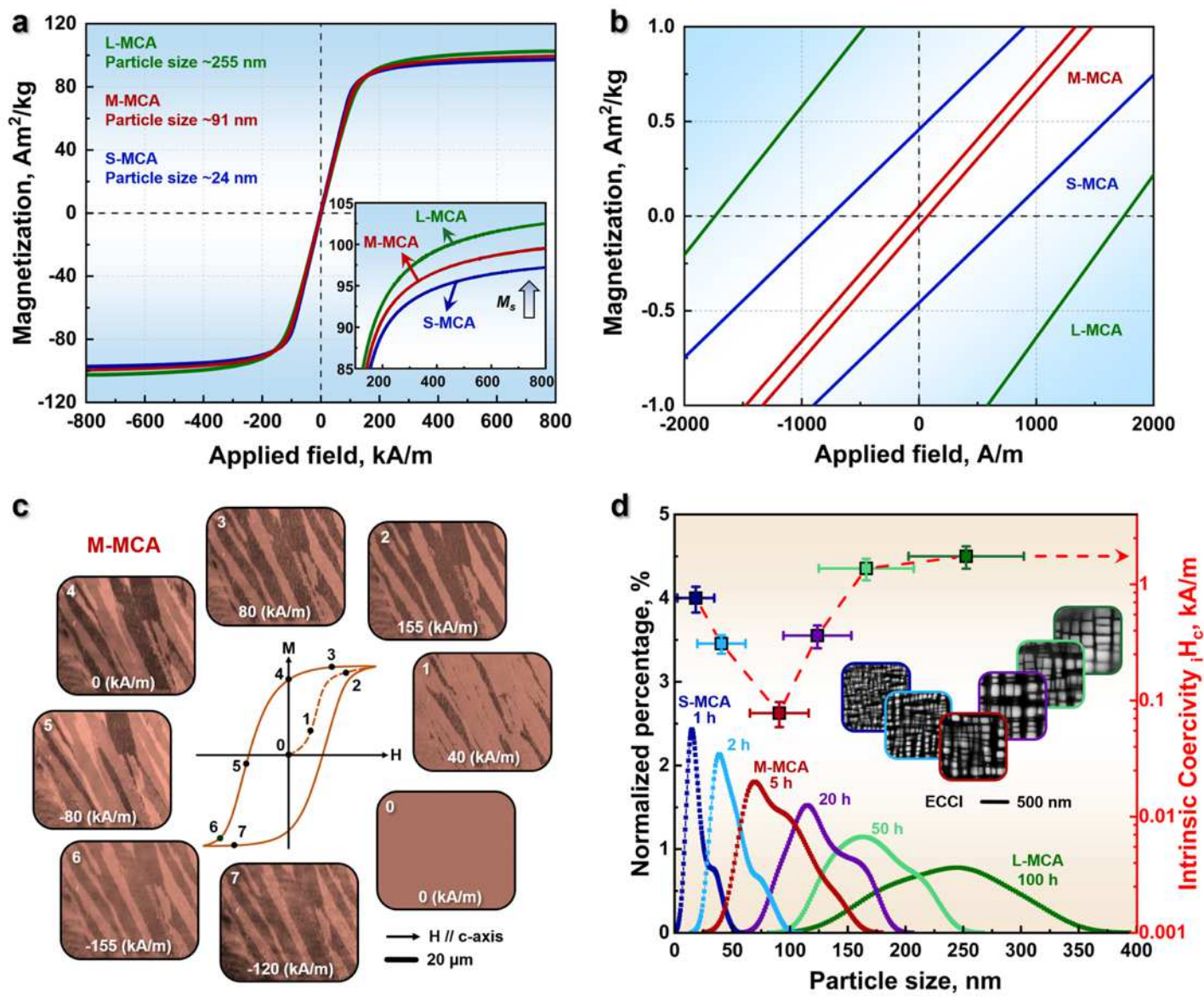


Figure 3

Soft magnetic response and associated Bloch wall motion behaviour of the MCAs at room-temperature. a, Hysteresis loops (M/H) acquired up to ± 800 kA/m. The magnetic field-sweeping rate is 1 kA/m. The inset shows the enlarged view of the increase in saturation magnetization with particle coarsening. b, M/H curves measured at a rate of 0.1 kA/m between ± 50 kA/m, showing the extremely low coercivity. c, MOKE microscopy observation, in longitudinal contrast, revealing the magnetization process. The applied magnetic field is horizontal to the viewing plane. d, Statistical particle size distribution of all the MCAs under different isothermal heat treatment conditions (1~100 h at 1173 K). The right inset shows the evolution of particle size by ECCI probing.

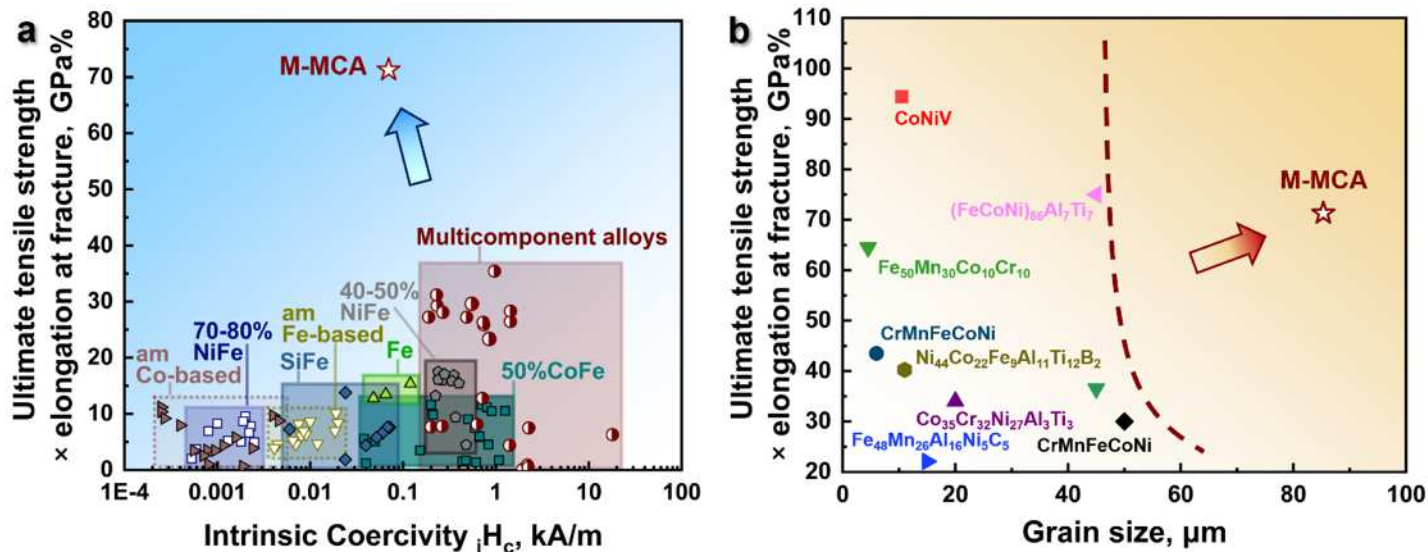


Figure 4

Mechanical and magnetic features combined in the new $\text{Fe}_{32}\text{Co}_{28}\text{Ni}_{28}\text{Ta}_5\text{Al}_7$ (at.%) M-MCA material. a, Ashby map compiling room-temperature ultimate tensile strength (σ_{UTS}) \times elongation at fracture (ϵ_f) and intrinsic coercivity compared to those of other soft magnetic materials, such as NiFe^{29,30}, CoFe^{31,32}, SiFe³³, Fe³⁴, amorphous alloys^{4,35-37} and established MCAs³⁸⁻⁴⁹. b, Ashby map showing $\sigma_{\text{UTS}}\times\epsilon_f$ versus average grain size compared to those of other strong and ductile MCAs^{22-24,50-53}. 'am' in the legend stands for amorphous alloys.

Supplementary Files

This is a list of supplementary files associated with this preprint. Click to download.

- [ExtendedData.docx](#)